communications
earth & environment

ARTICLE

https://doi.org/10.1038/s43247-021-00142-6 OPEN

Large-scale variation in seismic anisotropy in the crust and upper mantle beneath Anatolia, Turkey

Cédric P. Legendre [1✉], Li Zhao [2] & Tai-Lin Tseng [3]

The average anisotropy beneath Anatolia is very strong and is well constrained by shear-wave splitting measurements. However, the vertical layering of anisotropy and the contribution of each layer to the overall pattern is still an open question. Here, we construct anisotropic phase-velocity maps of fundamental-mode Rayleigh waves for the Anatolia region using ambient noise seismology and records from several regional seismic stations. We find that the anisotropy patterns in the crust, lithosphere and asthenosphere beneath Anatolia have limited amplitudes and are generally consistent with regional tectonics and mantle processes dominated by the collision between Eurasia and Arabia and the Aegean/Anatolian subduction system. The anisotropy of these layers in the crust and upper mantle are, however, not consistent with the strong average anisotropy measured in this area. We therefore suggest that the main contribution to overall anisotropy likely originates from a deep and highly anisotropic region round the mantle transition zone.

[1] Institute of Earth Sciences, Academia Sinica, Nangang, Taiwan. [2] School of Earth and Space Sciences, Peking University, Beijing, China. [3] Department of Geosciences, National Taiwan University, Taipei, Taiwan. ✉email: legendre@earth.sinica.edu.tw

Anatolia is a micro-plate between Eurasia and Arabia. Its tectonics is dominated by the collision of the Arabia and Eurasia plates on its eastern boundary (Fig. 1), which leads to the westward motion of the Anatolian Block, as constrained by Global Positioning System (GPS) measurements[1–3]. The extrusion of Anatolia is also greatly influenced by a complex subduction system in the eastern Mediterranean on its western and southern boundaries[4]. Anatolia is considered to be relatively simple in terms of deformation and can be explained by a simple block model, with a uniform pattern of westward ground velocity of the block[3,5]. Its northern frontier is the North Anatolia Fault, a right-lateral strike-slip boundary fault between the Anatolia and Eurasia plates, whereas its boundary with Arabia Plate is the left-lateral East Anatolian Fault[5]. The Anatolian Block has a more or less uniform crustal thickness of 40–50 km[6–8], and the thickness of lithosphere in the region is 80–100 km[9,10].

Seismic anisotropy in the crust is mostly attributed to the preferred orientation of anisotropic minerals, oriented cracks, lateral or vertical variations of compositions and structures[11,12]. In the upper mantle, seismic anisotropy is mainly attributed to stress or strain-induced alignment of anisotropic minerals[13–17], and has been used to infer the mantle flow and its relation with plate motions[18,19]. The SKS-based studies concluded that the anisotropic pattern is mostly controlled by a complex mantle flow, and the local perturbations originate from slab tears[19]. Seismic anisotropy can be deduced from laboratory experiments (elastic anisotropic behavior of rocks and minerals), numerical modeling (solution of the full elastic (anisotropy) wave equation), and seismological investigations[15,20,21]. In the Anatolia region, the fast axis derived by SKS/SKKS shear-wave splitting measurements[18] is rather homogeneous with a direction of N30°E (Fig. 1d). Other studies investigating the anisotropic structures of the region mostly focused on Pn polarization[22,23], providing the average anisotropy over the crust and upper lithosphere, or on surface-wave anisotropy of the crust[24]. Those studies found a complex anisotropic pattern within the upper crust, with mostly EW fast directions of anisotropy in eastern Anatolia, and NS to N170°E fast directions of anisotropy in western Anatolia.

Results and discussion

In this study, we investigate the vertical layering of anisotropy in the crust as well as the lithospheric and asthenospheric mantle beneath Anatolia by building maps of the fundamental-mode Rayleigh-wave phase velocity in the region using both ambient noise and teleseismic records from the available regional networks (Fig. S1). We adopt a two-station technique in measuring the interstation dispersion curves by cross-correlation approach (Figs. S2 and S3), resulting in a set of 1589 dispersion curves from ambient noise[24] and 2604 curves from teleseismic events (Fig. S4). Over 5750 teleseismic events were used to constrain our dispersion curves. Those events occurred between 1999 and 2015, with magnitude Mw > 5.5, located near the great circle linking two stations, and with an epicentral distance greater than ten times the interstation distance. Ambient noise cross-correlations of seismic records from regional networks provide measurements

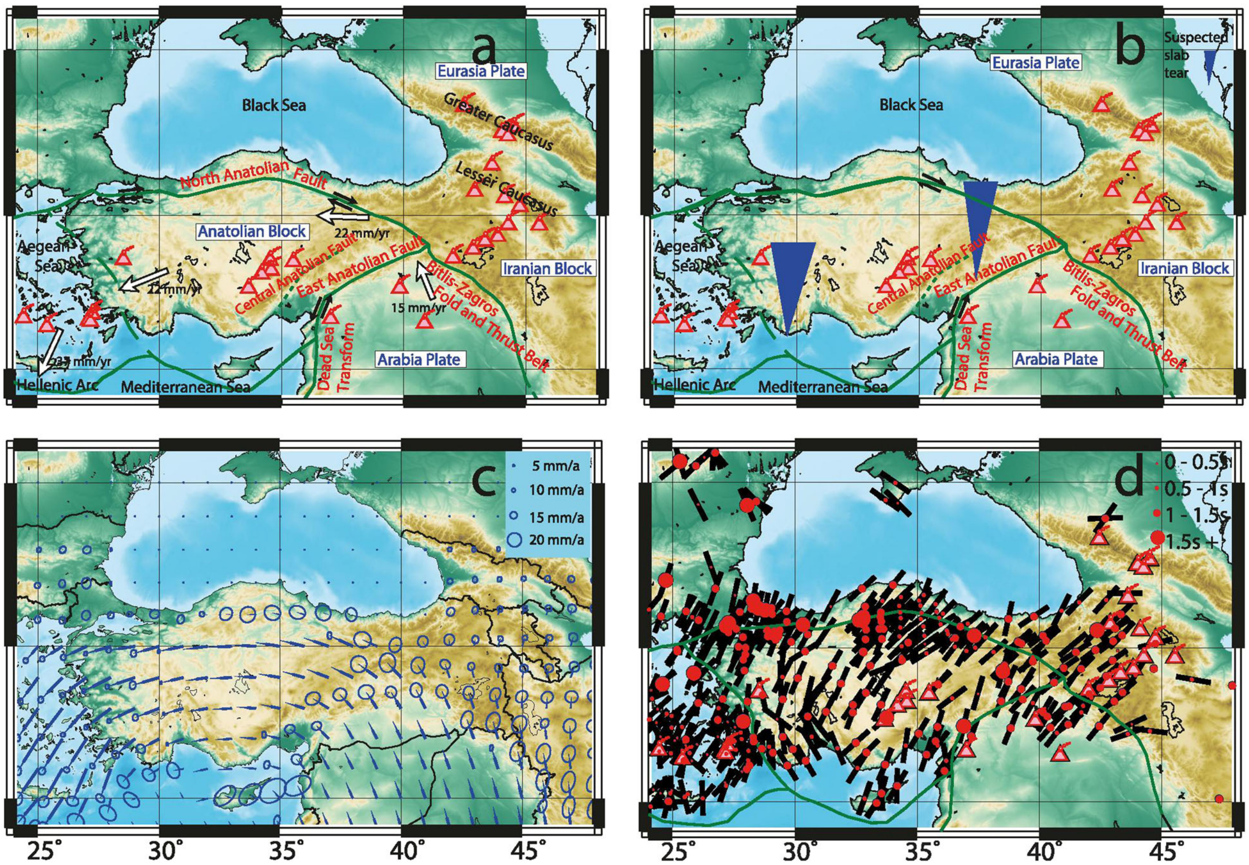

Fig. 1 Geodynamics of Anatolian Plate. a Regional tectonic map of Anatolia. Green lines are plate boundaries in the PB2002 model[60], and white arrows show velocity vectors of the Anatolia and Arabia plates relative to the Eurasia Plate[61]. Volcanoes[62] are displayed with pink triangles with vents. **b** Locations of the suspected slab tears (inverted blue triangles) beneath Anatolia[36]. **c** Surface velocity vectors (blue lines with uncertainty ellipses) extrapolated in and around the Anatolia Plate from GPS measurements[2]. **d** Seismic anisotropy estimated by SKS/SKKS shear-wave splitting measurements[18]. The black lines represent the fast directions of propagation, and the sizes of the red circles are proportional to the splitting times.

of short-period (5–25 s) dispersion curves, mostly sensitive to crustal and upper lithospheric structures[25,26]. We augment noise data with earthquake records to measure dispersion curves of longer periods (20–300 s), which are sensitive to the crust, lithosphere, and asthenosphere[27,28]. The overall period range is 5–300 s (Figs. 2 and S5), and the range of depth sensitivity of our dataset is 5–400 km.

We then invert the collection of dispersion curves for maps of both isotropic and azimuthally anisotropic anomalies of Rayleigh-wave phase velocity at selected periods (5–200 s every 5 s, and 210–300 s every 10 s)[29–31]. Parametrization and resolution are discussed in Supplementary Information (Figs. S6–S12). The resulting anisotropic Rayleigh-wave phase-velocity maps (Fig. S13) allow us to analyze the patterns of seismic anisotropy in

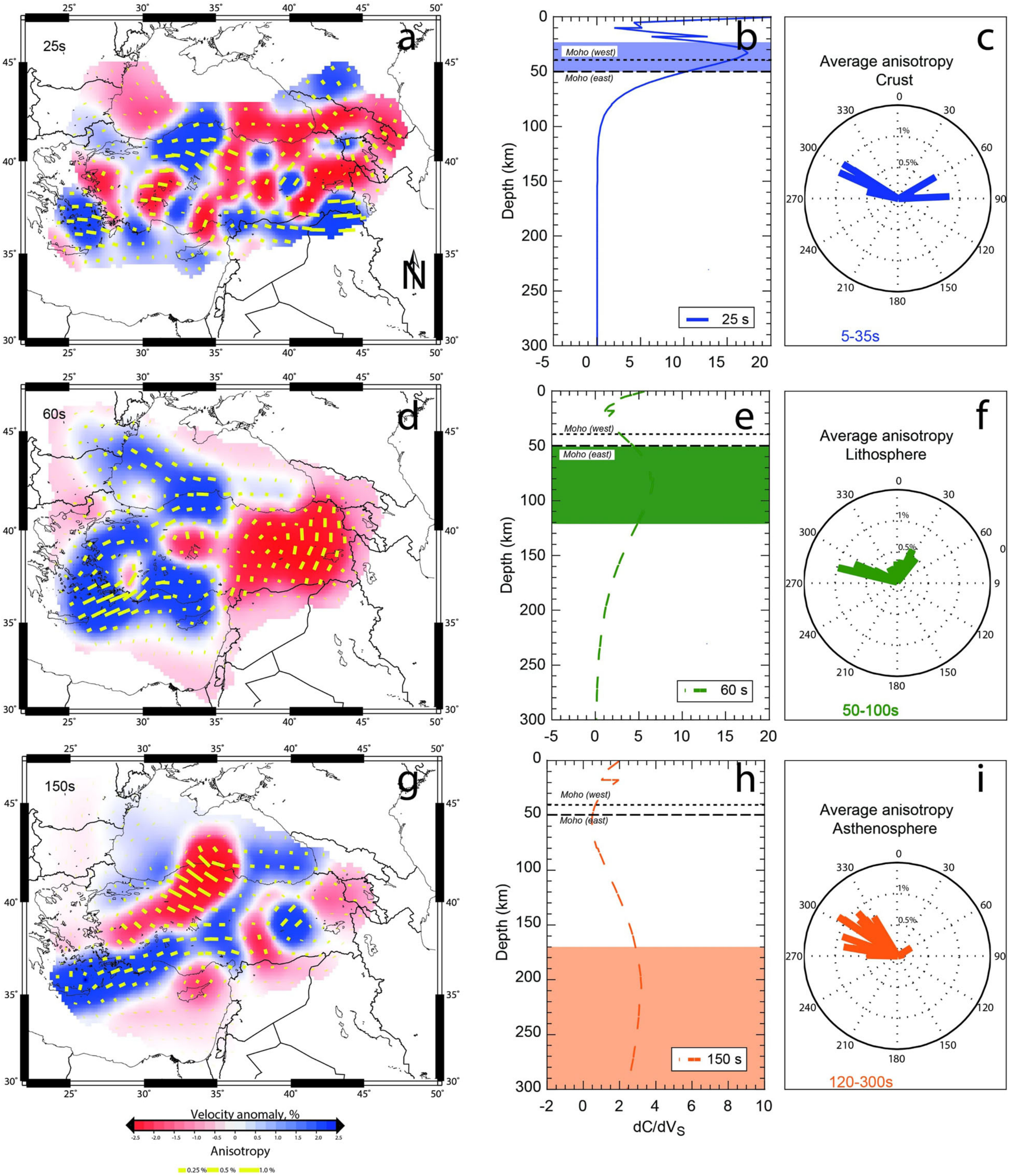

Fig. 2 Layering of seismic anisotropy at selected periods. Results of Rayleigh-wave phase velocity and anisotropy for the crust (25 s, **a**) and the lithospheric (60 s, **d**) and asthenospheric (150 s, **g**) mantle, with corresponding depth-dependent sensitivity kernels in (**b**), (**e**), and (**h**), respectively, in which the color-shaded areas indicate the estimated depth ranges of main sensitivity. The Moho depths beneath eastern and western Anatolia are also marked. Anisotropy averaged over the whole Anatolia region in crustal (5–35 s, **c**), lithospheric (50–100 s, **f**), and asthenospheric (120–300 s, **i**) mantle depth ranges.

different layers (Fig. S14) beneath Anatolia and understand possible contributions to the anisotropy.

Crustal anisotropy. The crustal thickness in Anatolia is mostly uniform, gradually changing from 27 km in the west to 50 km in the east[6–8,32–34]. This depth range is well sampled by Rayleigh waves of periods of 5–35 s (Fig. 2).

A recent study[24] has been focusing on the variations of crustal velocities and anisotropies derived from surface waves beneath Anatolia. Their results revealed a connection between the variations in isotropic and anisotropic crustal velocities and the locations of faults and melts. They also observed a general EW fast direction of anisotropy at large scale, supplemented by local variations in the anisotropic pattern.

In our updated model, large-scale patterns exhibit mostly EW-oriented fast axis of anisotropy in western, central, and souteastern Anatolia (Fig. 2a), which may be related to the westward extrusion of Anatolia and the stress induced in the crust. The average anisotropy (average azimuthal direction and average amplitude over all points in the model for a specific period) in the whole region in the period range of 5–35 s is mostly EW (Fig. 2c), inconsistent with the shear-wave splitting derived anisotropy orientation of N30°E (Fig. 1d), but in good agreement with the westward surface motion of Anatolia from GPS observations (Fig. 1c). The lateral variation observed in the crustal anisotropy pattern is also absent in the previous shear-wave splitting measurements (Fig. 1d). These discrepancies imply that the shear-wave splitting measurements in Anatolia are not strongly influenced by crustal structures, although considerable (non-negligible) contribution from the crustal structures on splitting measurements had been reported in other tectonic regions[35].

Lithospheric anisotropy. In the period band of 50–100 s, Rayleigh waves are mostly sensitive to depth range 50–120 km[28], they sample the lithospheric mantle. In this period range in our model, the anisotropic pattern is relatively simple (Fig. 2). A NS-oriented anisotropy, coupled with negative velocity anomaly, is present in eastern Anatolia and in the northern Arabian Plate, whereas the anisotropy in the region south of central and in western Anatolia shows a slightly different pattern, having mostly EW and NE-SW orientations with local variations that may be attributed to mantle heterogeneities. For instance, slab tears[36,37] are suspected to be present beneath Anatolia (Fig. 1b), and the probable locations of the slab tears are in good agreement with the velocity anomaly and the change in anisotropy in central Anatolia (37°E, 40°N in Fig. 2d), highlighted by a relatively strong heterogeneity in anisotropy in western Anatolia (29°E, 37°N in Fig. 2d and g).

Although the average anisotropy over the whole region we obtained in periods of 60–70 s is consistent with the shear-wave splitting measurements (Fig. 1d), other periods sampling the lithosphere (60 s and 80–100 s, Fig. S13) yield directions that are perpendicular to the anisotropy displayed by the shear-wave splitting measurements.

The most prominent feature at periods of 50–100 s is the strong dichotomy observed in our models. Beneath central and western Anatolia (Fig. 2d), EW anisotropy is present, whereas beneath eastern Anatolia and northern Arabia, mostly NS anisotropy is found (Figs. 2d and S13).

Such clear contrast is absent in the shear-wave splitting measurements (Fig. 1d). The strong dichotomy between Anatolia and Arabia in terms of anisotropy for periods of 50–100 s as well as the small-scale lateral variations of anisotropy would also rule out the lithosphere as the main contributor of the shear-wave splitting measurements in the region.

Our result also reveals a strong difference between the pattern of seismic anomaly and fast direction observed beneath Anatolia and Arabia for periods of 50–100 s. The N020°E direction of anisotropy beneath eastern Anatolia agrees well with the hypothesis of lithospheric delamination caused by the thermal erosion of the lithosphere in the region[38–40]. Beneath the northern Arabia Plate and eastern Turkey where North Anatolia Fault and East Anatolia Fault meet the Bitlis suture, a strong negative velocity anomaly is found (Figs. 2d and S13), indicating the presence of a warmer mantle or asthenospheric material. The slow anomaly is well correlated with the region of wide-spread post collisional volcanism[34,40], and the anisotropy appears stronger near eastern Turkey where the age of the volcanism is relatively young (≤6 Ma). The amplitudes of the anisotropy are rather limited in most parts of the region south of Bitlis and East Anatolia Fault, suggesting the presence of melts and probable vertical mantle flow. In our 2D tomographic inversion, vertical flow would have a predominant vertical component which would result in minor amplitudes in the horizontal components of the anisotropy. In Figs. 2d and g, around 37°E, where slab tear is proposed, limited amplitude of anisotropy might be explained by vertical flow.

Asthenospheric anisotropy. At periods sampling the asthenosphere (120–300 s, Fig. 2g), the anisotropic pattern shows a NW-SE orientation in the central and western parts of Anatolia, while in a small region in eastern Anatolia displays NE-SW orientation. In northwestern Anatolia, the anisotropic pattern is mostly of NW-SE orientation. The isotropic part of our model is still well consistent with previous P-wave tomographic studies in the depth range of 200–320 km[36]. In central and western Anatolia, in particular in the coastal areas, we observe a slight change in the anisotropic pattern, which is mostly in EW direction. Local variations of velocity and anisotropy may still be attributed to mantle heterogeneities, such as the Hellenic and Cyprean slabs and suspected slab tears (Fig. 1b). A major slab tear is thought to be present in central Anatolia (37°E, 40°N)[36]. Some small-scale perturbations of the anisotropic pattern and slow velocity anomaly in this area are also present in our model. In regions with fast velocities associated with subducting Aegean and Cyprus slabs (Figs. 2g and 3e), the anisotropy orientation is mostly NE-SW; whereas in regions with low velocities, potentially related to slab tears, the anisotropy is NW-SE. This may be linked to a mixture of horizontal flow in the region with a mantle toroidal flow in eastern Mediterranean, in addition to the vertical flow related to the slab system. The low-velocity anomaly beneath the presumed slab tears (37°E, 40°N and 29°E, 36°N) may be related to the upwelling of hot mantle in the complex slab system, which is also suggested by the anisotropic pattern. The presence of a slab tear may be supported by the toroidal flow in the asthenospheric mantle, indicated by a fan-shaped anisotropic pattern diverging near the tear (Fig. 3c). In the asthenosphere sampled by Rayleigh waves in the period band of 120–300 s, the average anisotropy in our model has a mostly NW-SE orientation (Fig. 2g–i), perpendicular to the NE-SW direction of anisotropy measured by shear-wave splitting, but in agreement with the average anisotropy in the region in the lithosphere (Fig. 2d and f). Therefore, it seems that the asthenosphere and lithosphere together in the upper mantle still make a limited contribution to the average anisotropy as measured by shear-wave splitting. The uniformly NE-SW direction of shear-wave splitting anisotropy in the whole region suggests that the source of anisotropy is probably deep from a large-scale process.

Origin of anisotropy. As shown in our Rayleigh-wave phase-velocity maps, small-scale lateral variations of the anisotropy in

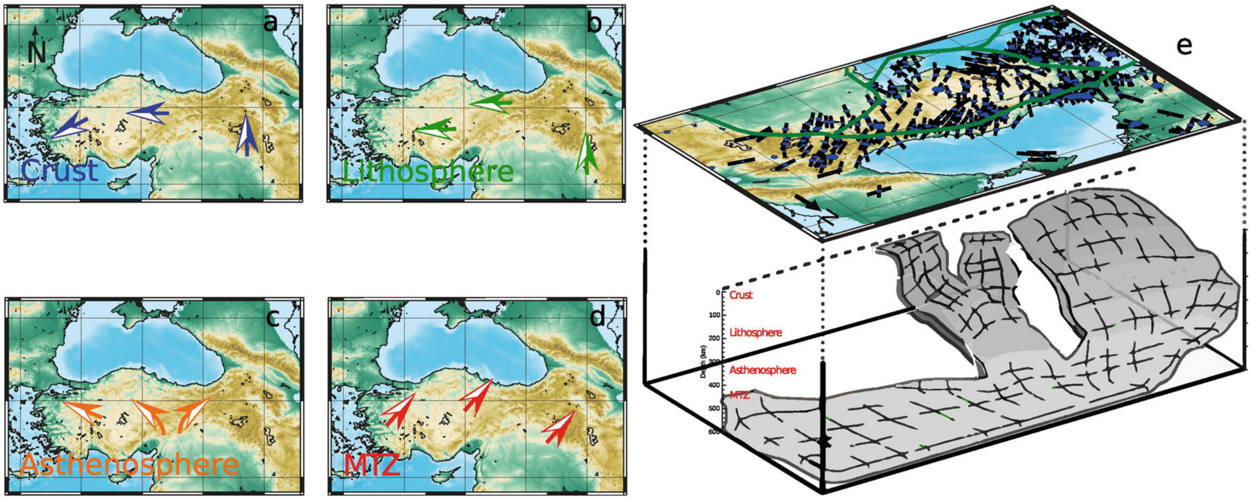

Fig. 3 Layering of seismic anisotropy in the crust and upper mantle. Sketches of the anisotropy in **a** the crust (blue arrows), **b** the lithosphere mantle (green arrows), **c** the asthenosphere mantle (orange arrows), and **d** the mantle transition zone (red arrows). **e** Perspective view of the shear-wave splitting measurements (black lines on the map) and the morphology of the slabs[36] under Anatolia.

the Anatolian crust as well as the underlying lithospheric and asthenospheric upper mantle are inconsistent with the largely uniform anisotropy pattern derived from shear-wave splitting measurements. On the other hand, large-scale patterns in the fast directions of anisotropy in the crust and upper mantle in our model are coherent and suggest that these two layers of anisotropy (crust and mantle) are coupled together. At periods of 3–35 s, sampling the crust, the fast direction of anisotropy is found to be mostly in EW direction for the whole region. In western Anatolia, similar EW directions of fast axis are found, at periods of 50–100 s, sampling the lithospheric mantle. In the asthenosphere, the fast directions of anisotropy are quite different from N120°E azimuth. In eastern Anatolia, beneath the Iranian Block and Arabia Plate, depth dependency in anisotropic fabric is also found between the crustal level (5–35 s) and the asthenospheric flow (sampled by periods >50 s) where lithosphere is likely thinner[32,41]. In our model shown in Figs. 2 and S13, the amplitude of anisotropy has a variation of 0.2–1.2% over the period band we investigated (5–300 s), with a mean value of about 1%. However, the shear-wave splitting measurements display a delay time of 1–1.5 s over the whole region. A 1% anisotropy over 40-km-thick crust would result in a delay time of 0.12 s, which is insignificantly small. Similarly, a 1% anisotropy over a 100-km-thick lithosphere and 270-km asthenosphere would result in delay times of 0.20 and 0.50 s, respectively. In order to explain the delay time of 1.5 s we need to have a consistent fast direction of anisotropy with an average anisotropy of ~3.2% over a 250-km-thick layer. This implies that the cause for the main anisotropic pattern observed by shear-wave splitting measurements should have a deep origin, with a long-wavelength signal and a very large lateral extension. One possible candidate shall be the remnant of previously subducted Tethyan lithosphere lying in the mantle transition zone[36,42–44]. The required anisotropy strength of over 3% is obtainable with the presence of olivine polymorphs and dense hydrous magnesium silicate as well as a limited amount of fluids[16,45–47], which is compatible with the presence of cold slabs[48] lying in the mantle transition zone[49,50]. Although the existence of α-olivine in the slabs in the Mediterranean region has never been confirmed, our result rules out the crust, lithosphere, and asthenosphere as the main contributor of anisotropy. Strong lateral variations of anisotropy are observed at those depths, which is inconsistent with the uniform pattern seen in shear-wave splitting measurements.

To reconcile our surface-wave results and the observed splitting data[47], we propose that there is a strong anisotropic layer within the mantle transition zone, probably the olivine polymorphs or dense hydrous magnesium silicate[51]. Strain-induced deformation and crystallographic orientation of bridgmanite in the uppermost lower mantle surrounding the slab is also another possible source[52,53], if the anisotropy can not be fully accommodated in the transition zone. Therefore, the current study provides plausible evidence for the existence of prominent anisotropy in the stagnant slabs at the bottom of the upper mantle beneath Anatolia.

The scenarios are likely that the specific orientation (N30°E) of the anisotropy within the slab could be explained by the frozen anisotropy preserved within the oceanic Tethyan lithosphere, or acquired anisotropy resulting from mantle flow within the transition zone[54–56].

Conclusion. In this study, we obtained the fundamental-mode Rayleigh-wave anisotropic phase-velocity maps for Anatolia from a combined dataset of ambient noise and earthquake records. Our model displays important features related to structural variations and dynamic processes in the region. Isotropic anomalies map the main tectonic blocks that are consistent with results from previous studies, whereas lateral and vertical variations of anisotropy provide additional constraints on the regional geodynamical evolution. In our anisotropic phase-velocity maps we resolve two distinct anisotropic layers beneath Anatolia, suggesting a mechanical decoupling between the crust and lithospheric mantle in this region. In the crust, the anisotropic pattern is in good agreement with the westwards extrusion of the Anatolia Plate as illustrated by GPS observations. On the other hand, the vertical continuity of the anisotropic patterns in the lithospheric and asthenospheric mantle beneath the Anatolia and Arabia plates, as well as small-scale local variations in the anisotropy, are inconsistent with the shear-wave splitting measurements, implying a deeper origin of the anisotropy. A uniform layer of anisotropy over the whole region is suggested to explain the delay times observed by shear-wave splitting measurements: a thick layer (≥250 km) with strong anisotropy (around 3%) is necessary, which argues for a remnant stagnant slab horizontally lying in the mantle transition zone beneath Anatolia, with the presence of highly anisotropic material such as α-olivine or hydrous magnesium silicate. Finally, our model also maps an anisotropy pattern consistent with a toroidal flow in the asthenospheric mantle combined with a strong velocity contrast in the presence of slab tear beneath eastern Anatolia.

Methods

In this study, we construct the anisotropic phase-velocity maps of fundamental-mode Rayleigh waves following a two-step approach. In the first step, we use the two-station method to measure the interstation Rayleigh-wave dispersion curve. For this purpose, three years (2015–2017) worth of vertical-component teleseismic waveforms at 142 seismic stations deployed in Anatolia are retrieved from IRIS-DMC (Incorporated Research Institutions for Seismology Data Management Center) and KOERI (Kandilli Observatory and Earthquake Research Institute), which offer relatively dense distribution of stations. This resulted in 2604 interstation dispersion curves with good coverage of the study region under the condition that the angle between the arc connecting a pair of stations and that connecting the earthquake and the station pair is less than 5 degrees. This dataset is further augmented by 1589 interstation dispersion curves (Fig. S1) derived from ambient noise[24], for a total of 4193 dispersion curves. To measure the interstation dispersion curve, vertical-component Rayleigh-wave records at a pair of stations are cross-correlated (Fig. S2). The cross-correlation function is filtered by a frequency-dependent Gaussian filter to minimize the effects of noise and interferences, and then transformed into the frequency domain where its complex phase is determined and used to estimate the phase velocity. For each station pair, phase velocities obtained from all earthquakes are assembled and the average dispersion curve as well as the standard deviation are calculated (Fig. S3). This approach allows us to obtain dispersion curves over the broad period range of 5–300 s. Bumps or portions of dispersion curves that are not smooth, measurements that do not agree with the average dispersion curve in terms of velocity, first and second derivatives, are considered as outliers and are discarded. The entire collection of dispersion curves are displayed in Fig. S4. After removal of outliers, the numbers of interstation pairs retained for phase-velocity map construction are different for different periods. Figure S5 shows the interstation path distribution for selected periods.

In the second step, we invert for the anisotropic phase-velocity maps at selected periods using the 3460 interstation dispersion curves. The anisotropic phase velocity at each point of the model can be expressed as follows[57]:

$$\delta C = \delta C_{\text{iso}} + A_{2\psi}\cos(2\psi) + B_{2\psi}\sin(2\psi) + A_{4\psi}\cos(4\psi) + B_{4\psi}\sin(4\psi). \quad (1)$$

Where δC_{iso} represent the isotropic phase-velocity perturbation, and the last four terms are the so-called 2ψ and 4ψ anisotropic anomalies. It has been shown that the 2ψ terms are 2–5 times larger than the 4ψ terms[24], and thus in our inversions, the 4ψ terms are not considered. This is also justified by the observation that the 4ψ terms are not necessary to explain the data since their inclusions in inversion have insignificant effect on χ^2 [58].

After deriving the dispersion curves for the 3460 interstation paths, we invert them for both isotropic and anisotropic (2ψ and 4ψ) Rayleigh-wave phase-velocity maps at selected periods. At each point of the model, the total velocity anomaly can be parameterized with five coefficients: one for the isotropic phase-velocity variation, δC_{iso}, 2 for the 2ψ-anomaly, $A_{2\psi}$ and $B_{2\psi}$, and 2 for the 4ψ-anomaly, $A_{4\psi}$ and $B_{4\psi}$.

In the inversion for Anatolia, we parameterize the model by a triangular grid of knots[43]. The grid spacing as well as the number of knots are variable with period depending on the interstation path coverage. At shorter periods (<30 s), the coverage is poorer with fewer paths, resulting in relatively large grid spacing and fewer knots over a reduced area (e.g., 78.226 km and 306 knots at 20 s). At longer periods, on the other hand, the coverage is better with more abundant path, leading to smaller grid spacing and more knots (e.g., 66.543 km and 425 knots at 80 s). The average interstation dispersion measured in the first step can be related to the local phase-velocity perturbation in Eq. (1) via an integral over the interstation arc:

$$\delta \bar{C}_i = \int_{\varphi}\int_{\theta} K_i(\varphi,\theta)\ \delta C(\varphi,\theta)\ d\theta\ d\varphi\ , \quad (2)$$

where $K_i(\varphi,\theta)$ is the sensitivity kernel.

In this study, we did not attempt to invert our dispersion curves into a 3D model. Therefore, sensitivity kernels used to estimate the depths of penetration of the surface waves at the periods investigated in this study are provided in Fig. S14.

Data availability

Dispersion curves and tomographic models are available at https://github.com/cplegendre/COMMSENV-20-0348.

Code availability

The codes used to compute the tomographic model and all derived results are available from the corresponding author upon reasonable request.

Received: 12 August 2020; Accepted: 16 March 2021;
Published online: 15 April 2021

References

1. McClusky, S., Reilinger, R., Mahmoud, S., Ben Sari, D. & Tealeb, A. GPS constraints on Africa (Nubia) and Arabia plate motions. *Geophys. J. Int.* **155**, 126–138 (2003).
2. Reilinger, R. et al. GPS constraints on continental deformation in the Africa-Arabia-Eurasia continental collision zone and implications for the dynamics of plate interactions. *J. Geophys. Res. Solid Earth* **111**, https://doi.org/10.1029/2005JB004051 (2006).
3. Allmendinger, R. W., Reilinger, R. & Loveless, J. Strain and rotation rate from GPS in Tibet, Anatolia, and the Altiplano. *Tectonics* **26**, https://doi.org/10.1029/2006TC002030 (2007).
4. van Hinsbergen, D. J., Kaymakci, N., Spakman, W. & Torsvik, T. H. Reconciling the geological history of western Turkey with plate circuits and mantle tomography. *Earth Planet. Sci. Lett.* **297**, 674–686 (2010).
5. Armijo, R., Meyer, B., Hubert, A. & Barka, A. Westward propagation of the North Anatolian Fault into the northern Aegean: timing and kinematics. *Geology* **27**, 267–270 (1999).
6. Gung, Y., Panning, M. & Romanowicz, B. Global anisotropy and the thickness of continents. *Nature* **422**, 707–711 (2003).
7. Vanacore, E., Taymaz, T. & Saygin, E. Moho structure of the Anatolian plate from receiver function analysis. *Geophys. J. Int.* **193**, 329–337 (2013).
8. Karabulut, H., Paul, A., Özbakír, A. D., Ergün, T. & Şentürk, S. A new crustal model of the anatolia–aegean domain: evidence for the dominant role of isostasy in the support of the anatolian plateau. *Geophys. J. Int.* **218**, 57–73 (2019).
9. Angus, D., Wilson, D. C., Sandvol, E. & Ni, J. Lithospheric structure of the Arabian and Eurasian collision zone in eastern Turkey from S-wave receiver functions. *Geophys. J. Int.* **166**, 1335–1346 (2006).
10. Kind, R. et al. Thickness of the lithosphere beneath Turkey and surroundings from S-receiver functions. *Solid Earth* **6**, 971–984 (2015).
11. Weiss, T., Siegesmund, S., Rabbel, W., Bohlen, T. & Pohl, M. Seismic velocities and anisotropy of the lower continental crust: a review. In *Seismic Exploration of the Deep Continental Crust*, 97–122 (Springer, 1999).
12. Dalton, C. A. & Gaherty, J. B. Seismic anisotropy in the continental crust of northwestern Canada. *Geophys. J. Int.* **193**, 338–348 (2013).
13. Zhang, S. & Karato, S.-I. Lattice Preferred Orientation of olivine aggregates deformed in simple shear. *Nature* **375**, 774–777 (1995).
14. Ekström, G. & Dziewonski, A. M. The unique anisotropy of the Pacific upper mantle. *Nature* **394**, 168–172 (1998).
15. Mainprice, D., Tommasi, A., Couvy, H., Cordier, P. & Frost, D. J. Pressure sensitivity of olivine slip systems and seismic anisotropy of Earth's upper mantle. *Nature* **433**, 731–733 (2005).
16. Karato, S.-i, Jung, H., Katayama, I. & Skemer, P. Geodynamic significance of seismic anisotropy of the upper mantle: new insights from laboratory studies. *Annu. Rev. Earth Planet. Sci.* **36**, 59–95 (2008).
17. Jung, H., Mo, W. & Green, H. W. Upper mantle seismic anisotropy resulting from pressure-induced slip transition in olivine. *Nat. Geosci.* **2**, 73–77 (2009).
18. Kaviani, A., Hatzfeld, D., Paul, A., Tatar, M. & Priestley, K. Shear-wave splitting, lithospheric anisotropy, and mantle deformation beneath the Arabia–Eurasia collision zone in Iran. *Earth. Planet. Sci. Lett.* **286**, 371–378 (2009).
19. Paul, A., Karabulut, H., Mutlu, A. K. & Salaün, G. A comprehensive and densely sampled map of shear-wave azimuthal anisotropy in the aegean–anatolia region. *Earth. Planet. Sci. Lett.* **389**, 14–22 (2014).
20. Bystricky, M., Kunze, K., Burlini, L. & Burg, J.-P. High shear strain of olivine aggregates: Rheological and seismic consequences. *Science* **290**, 1564–1567 (2000).
21. Confal, J. M., Faccenda, M., Eken, T. & Taymaz, T. Numerical simulation of 3-D mantle flow evolution in subduction zone environments in relation to seismic anisotropy beneath the eastern Mediterranean region. *Earth. Planet. Sci. Lett.* **497**, 50–61 (2018).
22. Al-Lazki, A. I. et al. Pn tomographic imaging of mantle lid velocity and anisotropy at the junction of the Arabian, Eurasian and African plates. *Geophys. J. Int.* **158**, 1024–1040 (2004).
23. Mutlu, A. K. & Karabulut, H. Anisotropic Pn tomography of Turkey and adjacent regions. *Geophys. J. Int.* **187**, 1743–1758 (2011).
24. Legendre, C., Tseng, T. & Zhao, L. Surface-wave phase-velocity maps of the Anatolia region (Turkey) from ambient noise tomography. *J. Asian Earth Sci.* **193**, 104322 (2020).
25. Shapiro, N. M., Campillo, M., Stehly, L. & Ritzwoller, M. H. High-resolution surface-wave tomography from ambient seismic noise. *Science* **307**, 1615–1618 (2005).
26. Legendre, C. P. et al. Complex deformation in the Caucasus region revealed by ambient noise seismic tomography. *Tectonophysics* **712**, 208–220 (2017).
27. Meier, T., Dietrich, K., Stöckhert, B. & Harjes, H.-P. One-dimensional models of shear wave velocity for the eastern Mediterranean obtained from the inversion of Rayleigh wave phase velocities and tectonic implications. *Geophys. J. Int.* **156**, 45–58 (2004).

28. Legendre, C. P., Deschamps, F., Zhao, L. & Chen, Q.-F. Rayleigh-wave dispersion reveals crust-mantle decoupling beneath eastern Tibet. *Sci. Rep.* **5**, 16644 (2015).
29. Lebedev, S., Meier, T. & van der Hilst, R. D. Asthenospheric flow and origin of volcanism in the Baikal rift area. *Earth Planet. Sci. Lett.* **249**, 415–424 (2006).
30. Endrun, B. et al. S velocity structure and radial anisotropy in the Aegean region from surface wave dispersion. *Geophys. J. Int.* **174**, 593–616 (2008).
31. Endrun, B., Lebedev, S., Meier, T., Tirel, C. & Friederich, W. Complex layered deformation within the Aegean crust and mantle revealed by seismic anisotropy. *Nat. Geosci.* **4**, 203–207 (2011).
32. Gök, R. et al. Lithospheric velocity structure of the Anatolian plateau-Caucasus-Caspian region. *J. Geophys. Res. Solid Earth* **116**, https://doi.org/10.1029/2009JB000837 (2011).
33. Salah, M. K. Lithospheric structure of southeast Anatolia from joint inversion of local and teleseismic data. *Stud. Geophys. Geod.* **61**, 703–727 (2017).
34. Lin, C.-M. et al. Locally thin crust and high crustal Vp/Vs ratio beneath the Armenian volcanic highland of the Lesser Caucasus: a case for recent delamination. *J. Geophys. Res. Solid Earth* **125**, e2019JB019151 (2020).
35. Barruol, G. & Mainprice, D. A quantitative evaluation of the contribution of crustal rocks to the shear-wave splitting of teleseismic SKS waves. *Phys. Earth. Planet. Inter.* **78**, 281–300 (1993).
36. Berk Biryol, C., Beck, S. L., Zandt, G. & Özacar, A. A. Segmented African lithosphere beneath the Anatolian region inferred from teleseismic P-wave tomography. *Geophys. J. Int.* **184**, 1037–1057 (2011).
37. Jolivet, L. et al. Aegean tectonics: strain localisation, slab tearing and trench retreat. *Tectonophysics* **597**, 1–33 (2013).
38. Kaviani, A. et al. Mantle Transition Zone thickness beneath the Middle East: evidence for segmented Tethyan slabs, delaminated lithosphere, and lower mantle upwelling. *J. Geophys. Res. Solid Earth* **123**, 4886–4905 (2018).
39. Lin, Y.-C. et al. Diachronous initiation of post-collisional magmatism in the Arabia-Eurasia collision zone. *Lithos* **356**, 105394 (2020).
40. Keskin, M. Magma generation by slab steepening and breakoff beneath a subduction-accretion complex: An alternative model for collision-related volcanism in eastern Anatolia, Turkey. *Geophys. Res. Lett.* **30** https://doi.org/10.1029/2003GL018019 (2003).
41. Şengör, A., Özeren, S., Genç, T. & Zor, E. East Anatolian High Plateau as a mantle-supported, north-south shortened domal structure. *Geophys. Res. Lett.* **30**, https://doi.org/10.1029/2003GL017858 (2003).
42. Spakman, W., van der Lee, S. & van der Hilst, R. Travel-time tomography of the European-Mediterranean mantle down to 1400 km. *Phys. Earth Planet. Inter.* **79**, 3–74 (1993).
43. Legendre, C., Meier, T., Lebedev, S., Friederich, W. & Viereck-Götte, L. A shear wave velocity model of the european upper mantle from automated inversion of seismic shear and surface waveforms. *Geophys.J. Int.* **191**, 282–304 (2012).
44. van der Meer, D. G., Van Hinsbergen, D. J. & Spakman, W. Atlas of the underworld: slab remnants in the mantle, their sinking history, and a new outlook on lower mantle viscosity. *Tectonophysics* **723**, 309–448 (2018).
45. Kawazoe, T. et al. Seismic anisotropy in the Mantle Transition Zone induced by shear deformation of wadsleyite. *Phys. Earth Planet. Inter.* **216**, 91–98 (2013).
46. Holtzman, B. et al. Melt segregation and strain partitioning: Implications for seismic anisotropy and mantle flow. *Science* **301**, 1227–1230 (2003).
47. Mainprice, D. & Ildefonse, B. Seismic anisotropy of subduction zone minerals–contribution of hydrous phases. in *Subduction Zone Geodynamics*, 63–84 (Springer, 2009).
48. Mosenfelder, J. L., Marton, F. C., Ross II, C. R., Kerschhofer, L. & Rubie, D. C. Experimental constraints on the depth of olivine metastability in subducting lithosphere. *Phys. Earth Planet. Inter.* **127**, 165–180 (2001).
49. Bina, C. R., Stein, S., Marton, F. C. & Van Ark, E. M. Implications of slab mineralogy for subduction dynamics. *Phys. Earth. Planet. Inter.* **127**, 51–66 (2001).
50. King, S. D., Frost, D. J. & Rubie, D. C. Why cold slabs stagnate in the Transition Zone. *Geology* **43**, 231–234 (2015).
51. Shieh, S. R., Mao, H.-k, Hemley, R. J. & Ming, L. C. Decomposition of phase D in the Lower Mantle and the fate of dense hydrous silicates in subducting slabs. *Earth Planet. Sci. Lett.* **159**, 13–23 (1998).
52. Tsujino, N. et al. Mantle dynamics inferred from the crystallographic preferred orientation of bridgmanite. *Nature* **539**, 81–84 (2016).
53. Ferreira, A. M., Faccenda, M., Sturgeon, W., Chang, S.-J. & Schardong, L. Ubiquitous Lower-Mantle anisotropy beneath subduction zones. *Nat. Geosci.* **12**, 301–306 (2019).
54. Audet, P. Seismic anisotropy of subducting oceanic uppermost mantle from fossil spreading. *Geophys. Res. Lett.* **40**, 173–177 (2013).
55. Eakin, C. M. et al. Internal deformation of the subducted Nazca slab inferred from seismic anisotropy. *Nat. Geosci.* **9**, 56–59 (2016).
56. Song, T.-R. A. & Kim, Y. Anisotropic uppermost mantle in young subducted slab underplating Central Mexico. *Nat. Geosci.* **5**, 55–59 (2012).
57. Smith, M. L. & Dahlen, F. The azimuthal dependence of Love and Rayleigh wave propagation in a slightly anisotropic medium. *J. Geophys. Res.* **78**, 3321–3333 (1973).
58. Deschamps, F., Lebedev, S., Meier, T. & Trampert, J. Azimuthal anisotropy of Rayleigh-wave phase velocities in the east-central United States. *Geophys. J. Int.* **173**, 827–843 (2008).
59. Wessel, P. & Smith, W. H. New version of the Generic Mapping Tools. *Eos, Trans. Am. Geophys. Union* **76**, 329–329 (1995).
60. Bird, P. An updated digital model of plate boundaries. *Geochem. Geophys. Geosys.* **4** https://doi.org/10.1029/2001GC000252 (2003).
61. Gripp, A. E. & Gordon, R. G. Current plate velocities relative to the hotspots incorporating the NUVEL-1 global plate motion model. *Geophys. Res. Lett.* **17**, 1109–1112 (1990).
62. Venzke, E. et al. Global volcanism, 1968 to the present. *Smithsonian Institution, Global Volcanism Program Digital Information Series, GVP-4* https://doi.org/10.5479/si.GVP.VOTW4-2013 (2002).

Acknowledgements

The facilities of IRIS Data Services, and specifically the IRIS Data Management Center, were used for access to waveforms, related metadata, and/or derived products used in this study. IRIS Data Services are funded through the Seismological Facilities for the Advancement of Geoscience (SAGE) Award of the National Science Foundation under Cooperative Support Agreement EAR-1851048. The facilities of Bogazici University Kandilli Observatory and Earthquake Research Institute Data Services (KOERI DS) were used for access to waveform and metadata required in this study. The KOERI DS is funded by the Ministry of Development of Turkey through the instrumentation and operation of the nationwide seismic network. Individual figure panels were generated with the Generic Mapping Tools[59]. Individual figure panels were combined using Inkscape (http://www.inkscape.org). C.L. was funded by the National Science Council of Taiwan under grants MOST 108-2811-M-001-572, 109-2116-M-001 -021 -MY3 & 109-2811-M-001 -608-. L.Z. has been funded by the National Natural Science Foundation of China (NSFC) under grant 41974046. T.L.T. was funded by the National Science Council of Taiwan under grant MOST 109-2116-M-002-027-.

Author contributions

C.P.L. performed the measurements and inversions, Z.L. and T.L.T. contributed to the interpretations and the writing and revision of the manuscript.

Competing interests

The authors declare no competing interests.

Additional information

Supplementary information The online version contains supplementary material available at https://doi.org/10.1038/s43247-021-00142-6.

Correspondence and requests for materials should be addressed to C.P.L.

Peer review information Primary handling editor: Joe Aslin.

Reprints and permission information is available at http://www.nature.com/reprints

Publisher's note Springer Nature remains neutral with regard to jurisdictional claims in published maps and institutional affiliations.